Influence of a Guide Field on Collisionless Driven Reconnection*)

Ritoku HORIUCHI[1,2), Shunsuke USAMI[1)] and Hiroaki OHTANI[1,2)]

[1)]*National Institute for Fusion Science, Toki 509-5292, Japan*
[2)]*The Graduate University for Advanced Studies, Toki 509-5292, Japan*

(Received 24 January 2014 / Accepted 19 April 2014)

The influence of a guide field on collisionless driven reconnection is investigated by means of two-dimensional electromagnetic particle simulation in an open system. In a quasi-steady state when reconnection electric field evolves fully, a current layer evolves locally in a narrow kinetic region and its scale decreases in proportion to an electron meandering scale as the guide field is intensified. Here, the meandering scale stands for an average spatial scale of nongyrotropic motions in the vicinity of the reconnection point. Force terms associated with off-diagonal components of electron and ion pressure tensors, which are originating from nongyrotropic motions of charged particles, becomes dominant at the reconnection point and sustain the reconnection electric field even when the guide field is strong. It is also found that thermalization of both ions and electrons is suppressed by the guide field. For the weak guide field, an electron nonthermal component is significantly created through a fast outburst from the kinetic region, while for the strong guide field, an ion nonthermal component is generated through the acceleration by an in-plane electric field near the magnetic separatrix.

Keywords: guide field, collisionless driven reconnection, meandering effect, energy conversion process

DOI: 10.1585/pfr.9.1401092

1. Introduction

It is widely believed that magnetic reconnection observed in various natural systems is controlled by common or similar physical processes, regardless of large differences in magnetic configurations and spatial-temporal scales [1]. A series of particle-in-cell (PIC) simulation studies has disclosed that that there are two microscopic mechanisms, which break a frozen-in condition and excite magnetic reconnection in a collisionless plasma without any guide field: one is due to anomalous resistivity associated with plasma instabilities [2–8] and the other is due to the effect of a nongyrotropic particle motion, called "meandering motion", in the vicinity of a reconnection point [9–13].

Because the amplitude of the meandering motion decreases with the guide field [14], it is expected that magnetic reconnection in a system with a strong guide field, such as fusion devices, may be altered from that in natural systems with no or a small guide field, such as solar corona and the earth's magnetosphere. To clarify the influence of the guide field on collisionless driven reconnection, Horiuchi and Sato [14] first applied a two-dimensional PIC simulation to a microscopic open system with the guide field, that was subject to an external driving flow. They found that under the influence of an external driving flow, an electron current layer thicness decreases with the guide field, and the reconnection rate is determined by the driving electric field. A series of numerical studies has extensively investigated the effect of a guide field on spontaneous reconnection [15–17]. The force term associated with the electron nongyrotropic pressure was found to play an important role in breaking electron frozen-in condition, even with a strong guide field.

Based on results from two-dimensional PIC simulations for an open system with an external driving source, the influences of a strong guide field on particle kinetic effects and energy conversion processes in collisionless driven reconnection are discussed in Sec. 2 and Sec. 3, respectively. Summary and discussion are given in Sec. 4.

2. Influence of a Guide Field on Particle Kinetic Effects

To clarify the influence of a guide field on collisionless driven reconnection, we have carried out a series of two-dimensional particle simulation runs in a microscopic open system, using "PASMO" code [9, 11, 12, 18]. The initial conditions used for these simulations were one-dimensional equilibrium with an antiparallel magnetic field along the x-axis and a uniform guide field along the z-axis,

$$B_x(y) = B_0 \tanh(y/L), \tag{1}$$

$$B_z(y) = B_{z0}, \tag{2}$$

$$P(y) = P_0 + \frac{B_0^2}{8\pi}\mathrm{sech}^2(y/L), \tag{3}$$

where B_0, B_{z0} and P_0 are constants and L is the scale height along the y-axis. The initial particle distribution was as-

author's e-mail: horiuchi.ritoku@nifs.ac.jp

*) This article is based on the invited talk at the 30th JSPF Annual Meeting (2013, Tokyo).

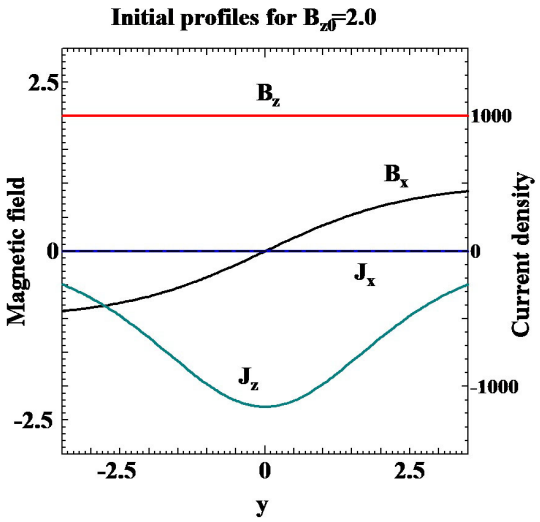

Fig. 1 Spatial profiles of magnetic field and current density in the initial state for $B_{z0}/B_0 = 2.0$, where the spatial scale is normalized by c/ω_{ce}.

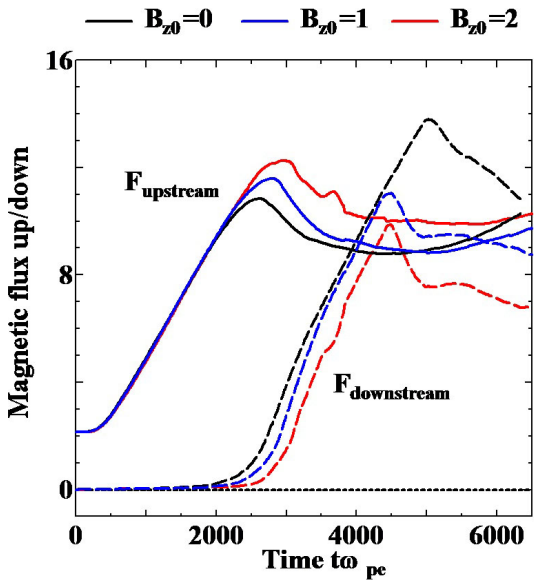

Fig. 2 Temporal evolutions of magnetic fluxes accumulated in the upstream (solid curves) and downstream (dashed curves) regions of a reconnection point for three different guide fields, $B_{z0}/B_0 = 0$(black), 1(blue), 2(red).

sumed to be a shifted Maxwellian with spatially constant temperature and average particle velocity equal to the diamagnetic drift velocity. Figure 1 shows the spatial profiles of the magnetic field and the current density along the y-axis in the initial condition for the case $B_{z0} = 2.0B_0$. An open boundary condition was adopted in the PASMO code. That is, an external driving electric field was imposed in the opposite z-direction at the upstream boundary ($y = \pm y_b$) to supply the particles into the simulation domain from the upstream boundary. The supplied particles satisfied the shifted Maxwellian with average velocity equal to $\boldsymbol{E} \times \boldsymbol{B}$ drift velocity. The downstream boundary ($x = \pm x_b$) was free, across which plasma could freely flow in or out. For this, it was assumed that the particle distribution was continuous across the downstream boundary [11, 18]. Thus, the total number of particles in the system changed with time, but the charge neutrality condition was always satisfied.

We carried out three simulation runs with different guide fields while keeping other simulation parameters the same; i.e., the total number of particles was 139, 673, 600, the simulation domain size was $2x_b \times 2y_b = 19.15\rho_{i0} \times 6.38\rho_{i0}$ (ρ_{i0}: initial ion Larmor radius defined using B_0), the ion-to-electron temperature ratio $T_i/T_e = 1$, the ion-to-electron mass ratio $m_i/m_e = 100$, the ratio of electron plasma frequency to electron gyration frequency $\omega_{pe}/\omega_{ce} = 6$, $L/\rho_{i0} = 2.1$, and the driving electric field imposed at the upstream boundary $E_d = -0.04B_0$. Figure 2 shows temporal evolutions of magnetic fluxes accumulated in the upstream (solid curves) and downstream (dashed curves) regions of a reconnection point for three different guide fields where black, blue, and red curves are results for $B_{z0}/B_0 = 0$, 1, and 2, respectively. Magnetic flux accumulates in the upstream region in the same manner regardless of the guide field strength until magnetic reconnection sets in. When the current layer is compressed as thin as ion kinetic scale, magnetic reconnection occurs and reconnected magnetic flux is carried away towards the downstream region by fast reconnection outflow [9, 11, 12]. As the guide field is intensified, the starting period of magnetic reconnection is delayed, and the maximum value of magnetic flux accumulated in the upstream increases. This suggests that the particle kinetic effect leading to excitation of magnetic reconnection strongly depends on the guide field and that the kinetic scale decreases as the guide field increases.

Figure 3 shows the current density profiles along the y-axis at $\omega_{pe}t = 5893$ for $B_{z0}/B_0 = 0$ (black), 1 (blue), and 2 (red). For comparison, the average amplitude of electron meandering motions, l_{me}, for each case is shown by a vertical dashed line, which is given by the distance from the reconnection point that satisfies

$$\rho_e(x_{rec}, y) = y. \tag{4}$$

Here x_{rec} is the x-coordinate of the reconnection point, and $\rho_e(x_{rec}, y)$ is the local electron Larmor radius defined using the total magnetic field $B = (B_x^2 + B_y^2 + B_z^2)^{1/2}$ and the electron temperature $T_{e,\perp}$ associated with the average electron thermal motion perpendicular to the local magnetic field. The current density is localized in a narrow region, and its scale decreases in proportion to the electron meandering scale. In other words, the current sheet evolves in the electron kinetic region, where unmagnetized meandering electrons predominantly exist, even with a strong guide field case. Note that a shoulder-like structure appears on the current density profile for $B_{z0}/B_0 = 1$. This phenomenon can be explained as follows. The electric current density

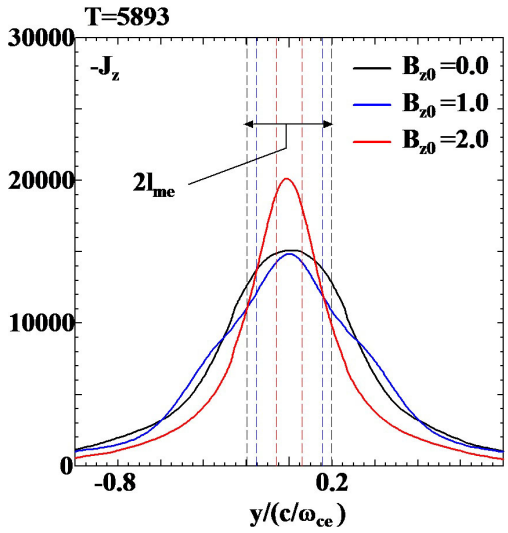

Fig. 3 Spatial profiles of the z-component of current density along the y-axis at $\omega_{pe}t = 5893$ for $B_{z0}/B_0 = 0$ (black curve), 1 (blue curve), and 2 (red curve). Vertical dashed lines indicate sizes of electron meandering orbits for each case.

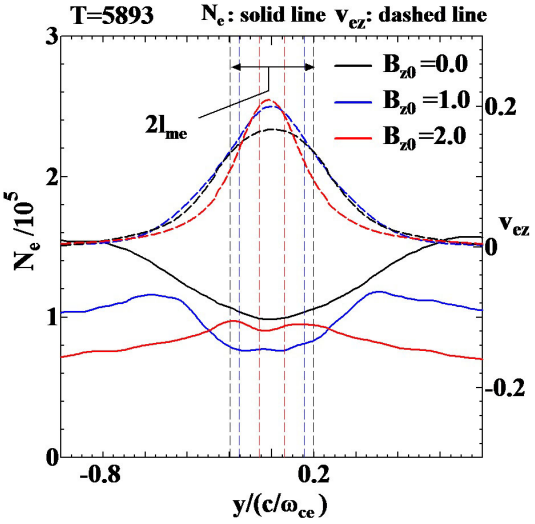

Fig. 4 Spatial profiles of the electron number density (solid) and the z-component of electron flow velocity (dashed) along the y-axis for the same conditions as in Fig. 3.

is mainly carried by electrons, and it is given by the product of number density and flow velocity. Figure 4 shows the spatial profiles of the electron number density (solid) and the z-component of electron flow velocity (dashed) along the y-axis for the same conditions as in Fig. 3. The depressed density profile appears in the central region of the current sheet due to complex meandering motions and convergent plasma inflows [11, 19], while the flow velocity profiles have similar structures with only one peak for each case. Especially, a clear shoulder structure is formed on the density profile for $B_{z0}/B_0 = 1$ (solid blue curve). Thus, the shoulder-like structure in the current density profile in Fig. 3 corresponds to that in the density profile in Fig. 4.

Figure 5 illustrates the spatial profiles of the current density, the z-component of the magnetic field, and the charge density in the xy-plane at $\omega_{pe}t = 5893$ for $B_{z0}/B_0 = 0$ and $B_{z0}/B_0 = 2$. For the strong guide field case the out-of-plane or the z-component of the magnetic field evolves dynamically into a complex form, which is controlled by the initial uniform guide field B_{z0}, the quadrupole field created by the Hall current, and compression by the external driving flow, as shown in Figs. 3 and 5. The current layer grows in a long and narrow region near the magnetic separatrix, and its shape becomes asymmetric against the vertical axis passing through a reconnection point, in contrast to that for a case with no guide field (Figs. 5-(a) and 5-(b)) [14]. Because the out-of-plane magnetic field in the strong guide field case consists of a symmetric guide field and quadrupole field created by the Hall current, the magnetic pressure decreases in the region where the sign of the quadrupole field is opposite to that of the guide field, while in the other region, the magnetic pressure increases. The external driving plasma flow strongly compresses the weak magnetic pressure region, and thus the asymmetric profile of the out-of-plane magnetic field is formed (Fig. 5-(d)). Strong compression creates an electron-rich region in the region of the weak magnetic field near the separatrix, where the electron current layer evolves (Figs. 5-(b) and 5-(e)).

Previous simulations with no guide field [10, 13, 19, 20] have disclosed that the effect of the meandering motion in the vicinity of a reconnection point plays a dominant role in breaking the plasma frozen-in condition and exciting collisionless reconnection. Let us consider how the microscopic mechanism responsible for collisionless reconnection is altered in the presence of the guide field. Here, it is useful to examine the non-ideal terms in the two-fluid equations,

$$\begin{aligned} \boldsymbol{E} + \boldsymbol{v}_j \times \boldsymbol{B} &= \frac{m_j}{q_j}\left(\frac{\partial}{\partial t} + \boldsymbol{v}_j \cdot \nabla\right)\boldsymbol{v}_j \\ &+ \frac{1}{n_j q_j}\left(\frac{\partial \bar{\boldsymbol{P}}_j}{\partial \boldsymbol{x}} + \frac{\partial p_j}{\partial \boldsymbol{x}}\right), \end{aligned} \tag{5}$$

where the subscript j (= i, e) denotes ion or electron, and $\bar{\boldsymbol{P}}_j$ and p_j are off-diagonal and diagonal components of the pressure tensor, respectively. The spatial profiles of the z-components of ideal and non-ideal terms in Eq. (5) are plotted in Fig. 6, where the top and bottom panels correspond to the profiles for electrons and ions, respectively, along the y axis at $\omega_{pe}t = 5893$ for the case of $B_{z0} = 2.0B_0$. The off-diagonal pressure tensor term (green curve) becomes dominant within a particle meandering scale (l_{mi} or l_{me}) in the vicinity of reconnection point ($y = 0$) and sustains the reconnection electric field (black curve) for both electrons and ions. These results are the same as those in the previous simulations with no guide field [9–12, 19] and are in good agreement with those from the simulation for

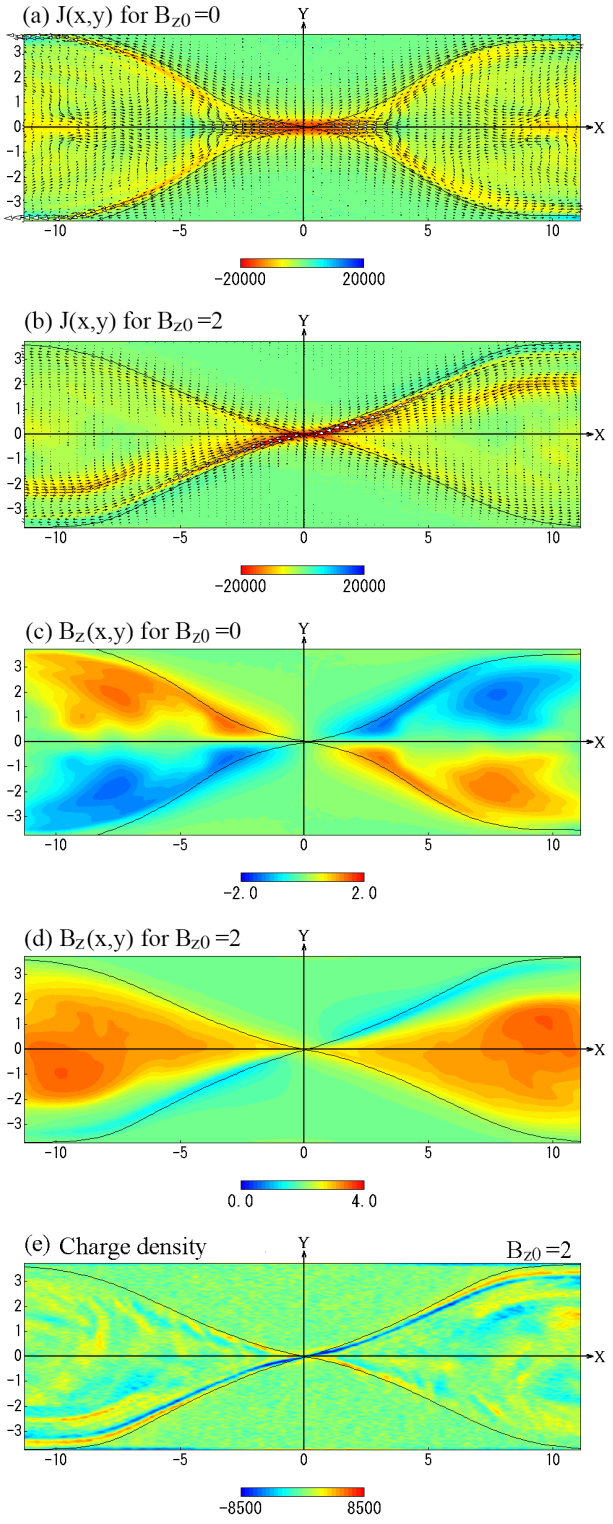

Fig. 5 Spatial profiles of (a) and (b) the current density, (c) and (d) the z-component of magnetic field, and (e) the charge density in the xy-plane at $\omega_{pe}t$ = 5893 for B_{z0}/B_0 = 0 in Panels (a) and (c) and B_{z0}/B_0 = 2 in Panels (b), (d), and (e). In the top two panels, color contours and vector plots stand for the z-component and xy-components of current density, respectively. The black curve represents the magnetic separatrix.

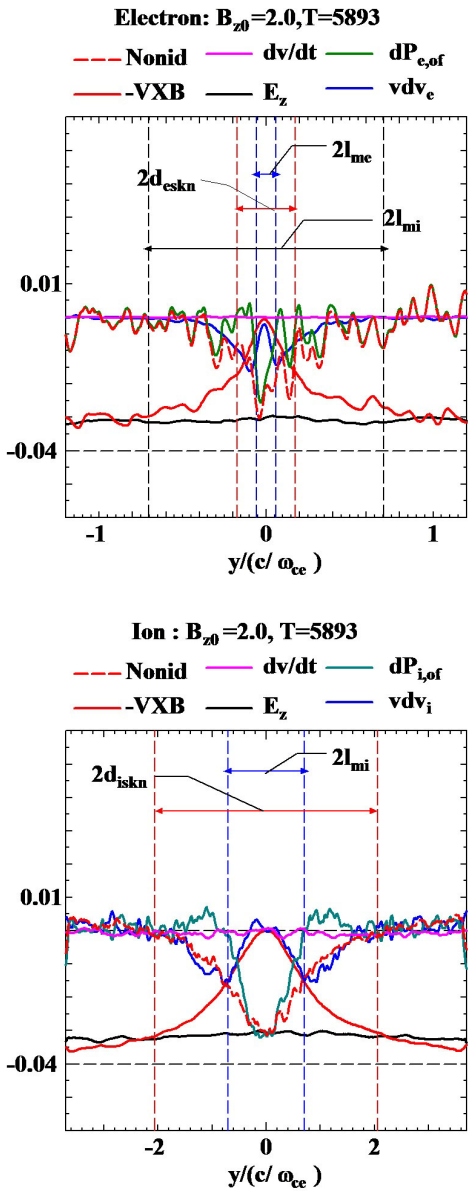

Fig. 6 Spatial profiles of the z-components of ideal and non-ideal terms in Eq. (5) at $\omega_{pe}t$ = 5893 for the case of B_{z0} = 2.0B_0. Top and bottom panels show the profiles for electrons and ions along the y-axis, respectively.

the strong guide field [14–16]. Since the off-diagonal components of pressure tensor terms originate from the meandering motion in the vicinity of a reconnection point, we conclude that the particle kinetic effect due to the meandering motion plays a key role in breaking the plasma frozen-in condition even when a strong guide field exists.

3. Influence of a Guide Field on Energy Conversion Processes

In the previous section, we have discussed the influence of a guide field on the particle kinetic effect as one of microscopic mechanisms that lead to breaking the

frozen-in condition and exciting collisionless reconnection. Through collisionless reconnection, fast energy conversion from magnetic field to particles also occurs as well as global change in magnetic field topology. In this section, we examine how the guide field affects the energy conversion process. Figure 7 shows the electron (top) and ion (bottom) energy spectra $F_{i/e}(\epsilon)$ at $\omega_{pe}t = 5893$ for $B_{z0}/B_0 = 0$ (black), and 2(red), where ϵ is the particle energy, and the energy spectrum $F_{i/e}(\epsilon)$ is defined by

$$\int F_{i/e}(\epsilon)d\epsilon = \text{total number of ions/electrons.} \quad (6)$$

For comparison, the thermal component of each spectrum, $F_t(\epsilon)$, is also plotted by dashed curves in Fig. 7. Here, the thermal component is given by a fitted curve for the thermal distribution as

$$F_t(\epsilon) = \alpha\sqrt{\epsilon}\exp(-\beta\epsilon), \quad (7)$$

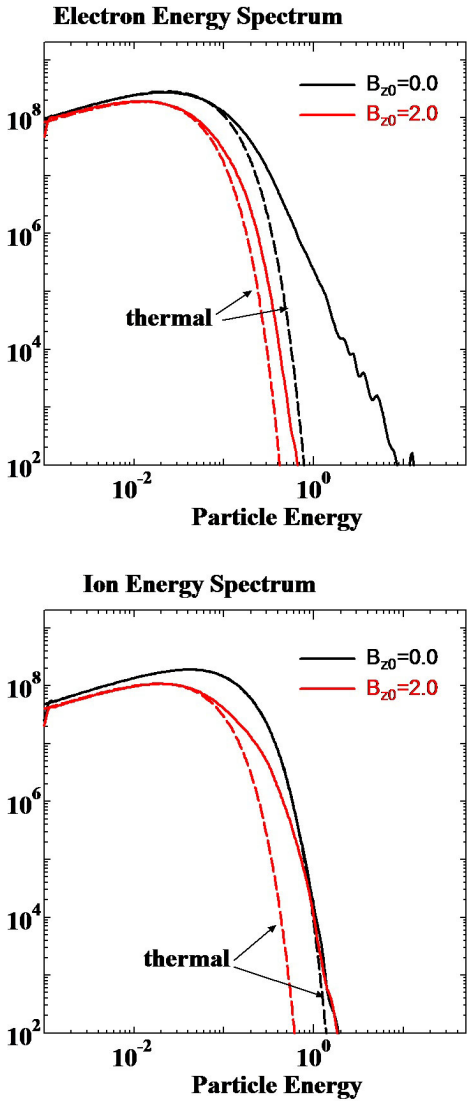

Fig. 7 Electron (top) and ion (bottom) energy spectra at $\omega_{pe}t = 5893$ for $B_{z0}/B_0 = 0$ (black), and 2(red). Dashed curves are the thermal component of each spectrum.

where α and β are fitting parameters and the fit was carried out using only the data in the energy region lower than that at the peak position of each spectrum.

Dissipation of magnetic field energy occurs inside a narrow electron kinetic region in the vicinity of the reconnection point. The thickness of the dissipation region scales as the meandering orbit amplitude, as discussed in Sec. 2. Therefore, as shown in Fig. 7, thermalization of both ions and electrons is suppressed to a lower level as the guide field is intensified. In contrast, the electron nonthermal component is observed significantly for the case of no guide field. To understand this phenomenon, we plot the electron distribution function F_e for $B_{z0}/B_0 = 0$ (top) and $B_{z0}/B_0 = 2$ (bottom) in the phase space (v_x, v_y) in Fig. 8, where electrons were sampled in the downstream region of the reconnection point within the size of area $\Delta x \times \Delta y = 4.99\rho_{e0} \times 3.33\rho_{e0}$ (ρ_{e0}: initial electron Larmor radius evaluated using B_0). As discussed in Sec. 2, unmagnetized meandering particle predominantly exists in the vicinity of the reconnection point. As the guide field intensifies, particles become magnetized and number of ummagnetized particles decreases. Unmagnetized particles are directly accelerated by the Hall electric field and the reconnection electric field. They not only form a fully developed current layer in the kinetic region but also provide a channel for fast electron outburst flowing towards the downstream. It is obviously seen in Fig. 8 that there exists a large deviation from the thermal distribution for $B_{z0}/B_0 = 0$, while the distribution changes to a compact structure consisting mainly of the thermal component for $B_{z0}/B_0 = 2$. This is the reason why the electron nonthermal component is observed significantly when no guide field is present. In contrast, for the strong guide field, the nonthermal component appears in the ion distribution. We will discuss the reason for this below.

Let us examine the energy conversion process in more detail. Figure 9 illustrates the combined spatial profiles of electron (blue and black) and ion (green and red) energy densities normalized by each number density for the same conditions as in Fig. 5, where the profiles in the upstream (negative y) and in the downstream (positive x) of a reconnection point ($(x, y) = (0, 0)$) are plotted. The left and right boundaries of the horizontal axis correspond to the upstream and downstream boundaries of the simulation box, respectively. Unmagnetized particles are accelerated directly by the Hall electric field and acquire energy inside the kinetic region. This acceleration amplifies the meandering motion. Because charged particles stay in the kinetic region for relatively longer times in the case of no guide field, the particle energy increases drastically when particles pass through the reconnection region (green and blue curves in Fig. 9). For a strong guide field case electrons are effectively accelerated in a narrow electron kinetic region because the reconnection electric field is parallel to the guide field there. Thus, a sharp peak appears in the electron kinetic energy around the reconnection point

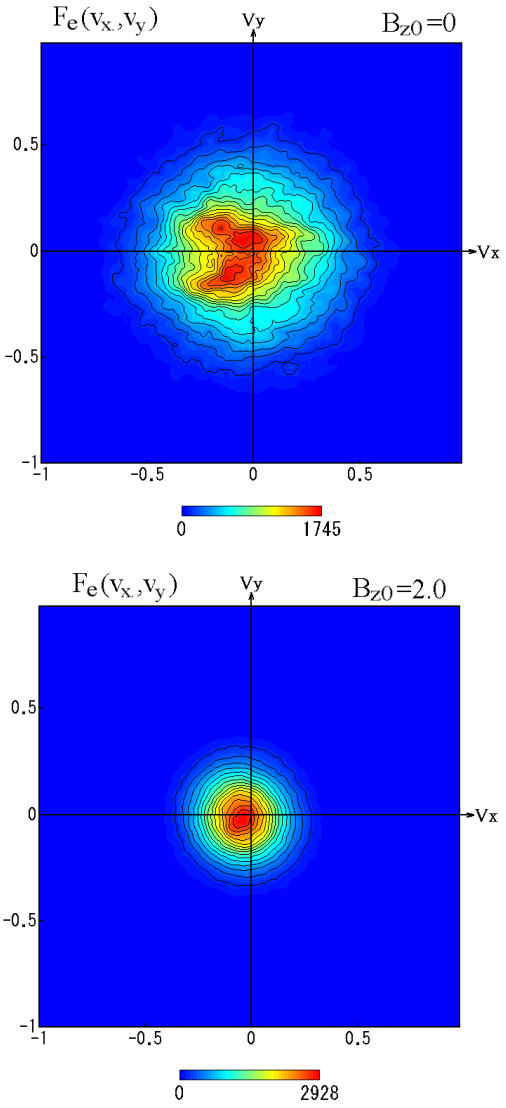

Fig. 8 Electron distribution functions at $\omega_{pe}t = 5893$ for $B_{z0}/B_0 = 0$ (top) and $B_{z0}/B_0 = 2$ (bottom) in phase space (v_x, v_y), where electrons were sampled around a point $(x, y) = (3.89\rho_{i0}, 0)$ in the downstream region. Electron velocity in the figure is normalized by the velocity of light.

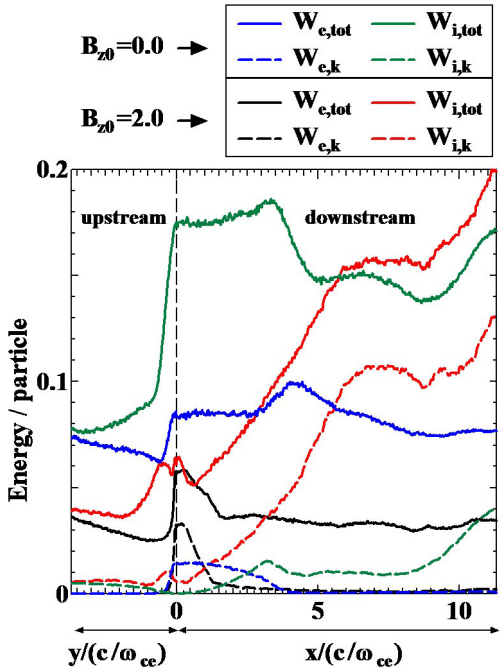

Fig. 9 Spatial profiles of electron and ion energies at $\omega_{pe}t = 5893$ for $B_{z0}/B_0 = 0$ (blue and green) and $B_{z0}/B_0 = 2$ (black and red) where the solid and dashed curves represent the profiles of total and kinetic energies per particle, respectively. The profiles in the upstream (negative y) and in the downstream (positive x) are combined at a reconnection point ($(x, y) = (0, 0)$).

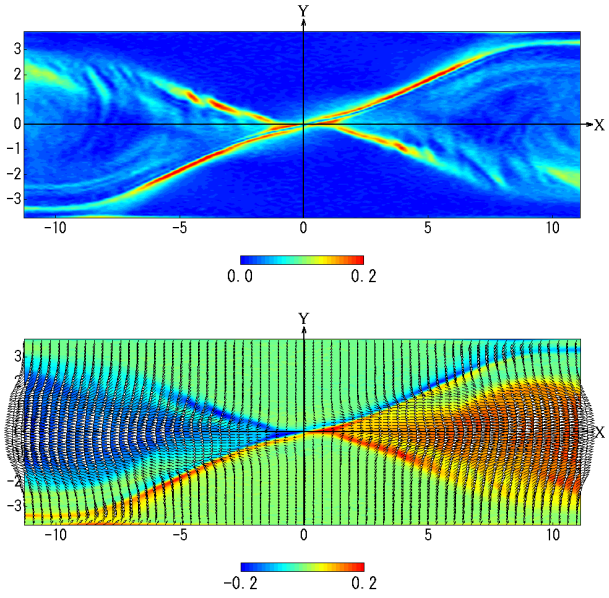

Fig. 10 Spatial profiles of (top) the function $|\boldsymbol{E} + \boldsymbol{v}_i \times \boldsymbol{B}|$ and (bottom) the y-component of electric field E_y and the in-plane component of ion flow velocity in the xy-plane at $\omega_{pe}t = 5893$ for $B_{z0}/B_0 = 2$, where color contours and vector plots in the bottom panel stand for electric field E_y and in-plane ion flow velocity (v_{ix}, v_{iy}), respectively.

(a black dashed curve in Fig. 9). The accelerated electrons move away from the reconnection region along the inclined current sheet (see Fig. 5-(b)). Note in Fig. 9 that for a strong guide field, ions, unlike electrons, obtain the kinetic energy mainly in the downstream region [21]. Let us consider how ions obtain kinetic energy there. Figure 10 shows the spatial profiles of the function $|\boldsymbol{E} + \boldsymbol{v}_i \times \boldsymbol{B}|$, the y-component of the electric field E_y and the in-plane component of the ion flow velocity in the xy-plane at $\omega_{pe}t = 5893$ for $B_{z0}/B_0 = 2$. The ion frozen-in condition is strongly violated near the magnetic separatirix mainly due to the in-plane component of the electric field ($|\boldsymbol{E} + \boldsymbol{v}_i \times \boldsymbol{B}| \neq 0$). Most of ions are supplied across the separatrix from the upstream to the downstream. When ions move across the sep-

aratrix, they are accelerated directly by the in-plane electric field towards the downstream region (bottom panel). Because the out-of-plane component of magnetic field is strongly amplified in the downstream region for a driven case (Fig. 5-(d)), ions are magnetized as soon as they move into the downstream (top panel). Thus, magnetized ions move towards the downstream boundary with fast outflow velocities. This ion outflow corresponds to the nonthermal component of the ion energy spectrum shown in Fig. 7. We conclude that for the weak guide field, a nonthermal component of electrons is significantly created through the fast electron outburst from the kinetic region, while for the strong guide field, a nonthermal component of ions is generated through the acceleration by the in-plane electric field near the magnetic separatrix.

4. Summary

We have investigated an influence of a guide field on collisionless driven reconnection by means of two-dimensional electromagnetic particle simulation in an open system. The reconnection current density evolves locally in the narrow electron kinetic region in which unmagnetized electrons exist, and the dissipation of magnetic energy predominantly occurs there. As the guide field is intensified, both the thickness of the current layer and the number of the unmagnetized electrons decrease in proportion to the electron meandering scale. The force terms associated with the off-diagonal components of electron and ion pressure tensors, which is originating from a nongyrotropic motion of charged particles, becomes dominant at the reconnection point and sustain reconnection electric field even when a strong guide field is present. We also found that in the presence of the guide field, thermalization of both ions and electrons is suppressed to a lower level because the dissipation region shrinks as the guide field is amplified. For a weak guide field, a nonthermal component of electrons is significantly created through a fast outburst from the kinetic region, while for a strong guide field, a nonthermal component of ions appears through the acceleration by an in-plane electric field near the magnetic separatrix.

As discussed in Sec. 1, there are two microscopic triggering mechanisms for collisionless reconnection. In this paper, we have focused on the influence of the guide field on the particle kinetic effect, based on the two-dimensional PIC simulation results. For complete understanding of collisionless reconnection, another important subject to be investigated is the role of anomalous resistivity associated with plasma instabilities in the presence of a strong guide field. Previous numerical simulation studies in the case of no guide field [4, 7, 8, 20] have demonstrated that anomalous resistivity is generated through the excitation of a drift kink instability [3] in the ion-scale current sheet after nonlinear modification of the current sheet by a lower hybrid drift instability [2]. However, it is easily expected that the anomalous resistivity associated with plasma instabilities is largely altered by a strong guide field. Because these plasma instabilities have a wavevector normal to the two-dimensional reconnection plane, three-dimensional analyses are needed to reach the complete understanding of collisionless driven reconnection in the presence of a strong guide field. This problem will be addressed in the near future.

Acknowledgments

The simulation was performed by employing the Plasma Simulator at the National Institute for Fusion Science. This study was partially supported by a Grant-in-Aid for Scientific Research from the Japan Society for the Promotion of Science (Grant No. 23340182), the Research Cooperation Program on "Hierarchy and Holism in Natural Sciences" at the National Institutes of Natural Sciences, and General Coordinated Research at the National Institute for Fusion Science (NIFS12KNSS028).

[1] M. Yamada, Rev. Mod. Phys. **82**, 603 (2010).
[2] N.A. Krall and P.C. Liewer, Phys. Rev. **4**, 2094 (1971).
[3] Z. Zhu and R.M. Winglee, J. Geophys. Res. **101**, 4885 (1996).
[4] R. Horiuchi and T. Sato, Phys. Plasmas **6**, 4565 (1999).
[5] W. Daughton, Phys. Plasmas **6**, 1329 (1999).
[6] W. Daughton, G. Lapenta and P. Ricci, Phys. Rev. Lett. **93**, 105004 (2004).
[7] T. Moritaka, R. Horiuchi and H. Ohtani, Phys. Plasmas **14**, 102109 (2007).
[8] T. Moritaka and R. Horiuchi, Phys. Plasmas **15**, 092114 (2008).
[9] R. Horiuchi and T. Sato, Phys. Plasmas **1**, 3587 (1994).
[10] M. Hesse, K. Schindler, J. Birn and M. Kuznetsova, Phys. Plasmas **6**, 1781 (1999).
[11] W. Pei, R. Horiuchi and T. Sato, Phys. Plasmas **8**, 3251 (2001).
[12] W. Pei, R. Horiuchi and T. Sato, Phys. Rev. Lett. **87**, 235003 (2001).
[13] R. Horiuchi and H. Ohtani, Comm. Comp. Phys. **4**, 496 (2008).
[14] R. Horiuchi and T. Sato, Phys. Plasmas **4**, 277 (1997).
[15] M. Hesse, M. Kuznetsova, K. Schindler and J. Birn, Phys. Plasmas **12**, 100704 (2005).
[16] M. Hesse, Phys. Plasmas **13**, 122107 (2006).
[17] P. Pritchett, Phys. Plasmas **12**, 062301 (2005).
[18] H. Ohtani and R. Horiuchi, Plasma Fusion Res. **4**, 024 (2009).
[19] A. Ishizawa and R. Horiuchi, Phys. Rev. Lett. **95**, 045003 (2005).
[20] R. Horiuchi, S. Usami, H. Ohtani and T. Moritaka, Plasma Fusion Res. **5**, S2006 (2010).
[21] S. Inoue, Y. Ono, R. Horiuchi, H. Ohtani, S. Usami, Y. Kaminou and K. Yamasaki, Proc. 24th IAEA-FEC (2014), to be published.